

Transparent Boundary Conditions for the Time-Dependent Schrödinger Equation with a Vector Potential

Jason Kaye *

Leslie Greengard †

Abstract

We consider the problem of constructing transparent boundary conditions for the time-dependent Schrödinger equation with a compactly supported binding potential and, if desired, a spatially uniform, time-dependent electromagnetic vector potential. Such conditions prevent nonphysical boundary effects from corrupting a numerical solution in a bounded computational domain. We use ideas from potential theory to build exact nonlocal conditions for arbitrary piecewise-smooth domains. These generalize the standard Dirichlet-to-Neumann and Neumann-to-Dirichlet maps known for the equation in one dimension without a vector potential. When the vector potential is included, the condition becomes non-convolutional in time. For the one-dimensional problem, we propose a simple discretization scheme and a fast algorithm to accelerate the computation.

This is the second version of the manuscript, correcting an important omission: namely the paper [1], which derived exact transparent boundary conditions from Green's representation theorem, as we do in Section 2 below. We have made minor changes to the presentation, emphasizing that the novelty of the present work is in the derivation of a fast algorithm which makes the Green's function-based approach practical.

1 Introduction

We begin with the time-dependent Schrödinger equation in free space, given by

$$\begin{aligned} iu_t(x, t) &= -\Delta u(x, t) + i\mathbf{A}(t) \cdot \nabla u(x, t) + V(x, t) u(x, t), & x \in \mathbb{R}^d, \quad t \in [0, T], \\ u(x, 0) &= u_0(x), \\ |u(x, t)| &\rightarrow 0, & |x| \rightarrow \infty. \end{aligned} \tag{1}$$

Here, $u(x, t)$ represents a complex-valued wave function, $u_0(x)$ is the given initial data, and $V(x, t)$ is a binding potential, and $\mathbf{A}(t)$ is an applied electromagnetic vector potential. We assume that $u_0(x)$ and $V(x, t)$ are supported in a bounded domain Ω in \mathbb{R}^d . In order to solve (1) on Ω alone, one must impose conditions on the boundary $\partial\Omega$ so that the solution of the corresponding equation matches the solution to the free space problem with sufficient precision. Such conditions are referred to by several names, including *absorbing boundary conditions*, *artificial boundary conditions*, and *non-reflecting boundary conditions*. Their purpose is typically to prevent spurious reflections of outgoing waves from $\partial\Omega$ (but see Remark 1 below). We refer to a boundary condition

$$\mathcal{B}[u](x, t) = 0, \quad x \in \partial\Omega$$

as an exact *transparent boundary condition* (TBC) when the solution of

$$\begin{aligned} iu_t(x, t) &= -\Delta u(x, t) + i\mathbf{A}(t) \cdot \nabla u(x, t) + V(x, t) u(x, t), & x \in \Omega, \quad t \in [0, T], \\ \mathcal{B}[u](x, t) &= 0, & x \in \partial\Omega, \\ u(x, 0) &= u_0(x) \end{aligned} \tag{2}$$

*Courant Institute of Mathematical Sciences, New York University, New York, NY 10012. (Email: jkaye@cims.nyu.edu).

†Courant Institute of Mathematical Sciences, New York University, New York, New York 10012 and Flatiron Institute, Simons Foundation, New York, New York 10010. (Email: greengard@cims.nyu.edu).

is equal to the solution of (1), restricted to Ω .

Exact TBCs for a variety of linear and nonlinear wave propagation problems have been studied extensively. They are typically nonlocal in space and time, so that fast and memory-efficient algorithms are required for their use in large problems. For the free space Schrödinger equation with $\mathbf{A}(t) = 0$, TBCs are known in certain domains, and several fast algorithms are available. For $d = 1$, Baskakov and Popov [2] derived an exact condition which takes the form of a history-dependent Dirichlet-to-Neumann map and may be discretized as a Robin condition. Fast algorithms to implement this condition were introduced in [3, 4, 5]. In higher dimensions, TBCs have been derived for the circle, sphere, and half-space using a spectral decomposition of the solution in space, and either a Laplace transform in time or appropriate special functions [6, 7, 8, 9, 10]. Fast algorithms applicable to these conditions are related to those developed for the one-dimensional case [4, 5, 7]. A similar approach for general domains was introduced in [11], but the conditions are given in the Laplace transform domain, and efficiently recovering time domain conditions is not straightforward. Half-space conditions were derived by a different method in [12, 13, 14], and used to assemble conditions for a rectangle in $d = 2$ and a box in $d = 3$. These are written in terms of auxiliary unknowns, obtained by solving lower-dimensional Schrödinger equations on boundary faces and edges. Fast algorithms for this approach were not considered. In another class of methods, exact TBCs have been developed directly for particular discretizations of the Schrödinger equation. Examples include [15] for a waveguide geometry, which is closely related to the one-dimensional case, [16] for the circle, and [17] for the rectangle.

For the case $\mathbf{A}(t) \neq 0$, there are fewer results. In [18], TBCs were presented for $d = 1$ with some restrictions on the vector potential, and the fast algorithm of [4] was adapted to the conditions. More general TBCs for $d = 1$ were presented in [19] without a fast algorithm. In [1], the full Green's function was derived for any dimension, and it was observed that exact TBCs follow from Green's representation theorem, although no fast algorithms were described. We use this approach below and show how exact TBCs for (1), with or without a vector potential, are easily obtained for arbitrary piecewise-smooth domains in any dimension. A byproduct of the potential theory formulation is that we obtain a representation of the solution which may be evaluated anywhere in the exterior domain $\mathbb{R}^d \setminus \Omega$, if desired. While the integral operators involved in the conditions are convolutional in time when $\mathbf{A}(t) = 0$, this is not true otherwise. For the one-dimensional case, we introduce a new class of fast algorithms to apply these nonlocal, non-convolutional operators.

Finally, we note that there are many methods used to prevent boundary reflections without implementing exact TBCs. Their purpose is to avoid the complexity associated with exact nonlocal conditions, or to mimic an exact condition when none is known. For the Schrödinger equation, they include the method of mask functions, perfectly matched layers, exterior complex scaling, approximate absorbing boundary conditions based on pseudodifferential calculus, and splitting methods. We do not discuss these approaches here, but refer the reader to [10, 20, 21, 22, 23] and the references therein.

Remark 1. *The vector potential term in (1) represents an applied electromagnetic field, and causes advection of the solution. Therefore, depending on its form, this term may cause waves which have left the domain Ω to return later. This poses a challenge for the various approximate absorbing boundary conditions in common use, which, in essence, assume that waves crossing $\partial\Omega$ are always outgoing. The TBCs we derive do not involve such an assumption, as will be demonstrated in our numerical results.*

The paper is organized as follows. In section 2, we introduce the relevant aspects of potential theory for the Schrödinger equation and derive exact TBCs. In section 3, we describe a simple numerical implementation of the exact condition in the one-dimensional case. In section 3.1, we discuss a fast algorithm for evaluating the nonlocal, non-convolutional integral operators which appear in the TBC when the vector potential is present. In section 4, we illustrate the performance of our method with several numerical examples, and in section 5, we mention a few directions for future work.

2 Derivation of TBCs by potential theory

In the absence of the binding potential and the vector potential, the wave function satisfies the free-particle Schrödinger equation,

$$iu_t = -\Delta u, \tag{3}$$

whose Green's function [24] is given by

$$K(x, t) = \frac{e^{i|x|^2/4t}}{(4\pi it)^{d/2}}.$$

Using this Green's function, we can define single and double layer potentials with densities σ and μ , respectively, on a spacetime boundary. In one dimension, these take the form

$$\mathcal{S}[\sigma](x, t) := \int_0^t K(x - x_0, t - s) \sigma(s) ds = \frac{1}{\sqrt{4\pi i}} \int_0^t \frac{e^{i(x-x_0)^2/4(t-s)}}{\sqrt{t-s}} \sigma(s) ds, \quad (4)$$

$$\mathcal{D}[\mu](x, t) := \int_0^t \frac{\partial K}{\partial x}(x - x_0, t - s) \mu(s) ds = \frac{\sqrt{i}}{4\sqrt{\pi}} \int_0^t (x - x_0) \frac{e^{i(x-x_0)^2/4(t-s)}}{(t-s)^{3/2}} \mu(s) ds, \quad (5)$$

for the boundary point $x = x_0$. The single layer potential is continuous, and the double layer potential satisfies the jump condition

$$\lim_{x \rightarrow x_0^\pm} \mathcal{D}[\mu](x, t) = \pm \frac{i}{2} \mu(t). \quad (6)$$

For $d > 1$ and $\partial\Omega$ piecewise-smooth,

$$\mathcal{S}[\sigma](x, t) := \int_0^t \int_{\partial\Omega} K(x - y, t - s) \sigma(y, s) dS(y) ds, \quad (7)$$

$$\mathcal{D}[\mu](x, t) := \int_0^t \int_{\partial\Omega} \frac{\partial K}{\partial \nu_y}(x - y, t - s) \mu(y, s) dS(y) ds. \quad (8)$$

Here and throughout, ν denotes a unit outward normal with respect to the domain Ω . The single layer potential is again continuous, and the jump condition for the double layer potential is similar to that for the parabolic case [25],

$$\lim_{\epsilon \rightarrow 0^+} \mathcal{D}[\mu](x_0 \pm \epsilon \nu_{x_0}, t) = \mp \frac{i}{2} \mu(x_0, t) + \mathcal{D}^*[\mu](x_0, t), \quad (9)$$

for $x_0 \in \partial\Omega$, excluding non-smooth boundary points, where $\mathcal{D}^*[\mu]$ is the principal value of $\mathcal{D}[\mu]$.

When the vector potential is non-zero, the governing equation is

$$iu_t = -\Delta u + i\mathbf{A}(t) \cdot \nabla u. \quad (10)$$

In one dimension, $A(t)$ is a scalar and we have

$$iu_t = -u_{xx} + iA(t)u_x. \quad (11)$$

Let $\varphi(t)$ be the indefinite integral of $\mathbf{A}(t)$ (or $A(t)$)

$$\varphi(t) = \int_0^t \mathbf{A}(s) ds.$$

It is straightforward to verify that if $u(x, t)$ satisfies (3), then $u(x + \varphi(t), t)$ satisfies either (10) or (11), depending on the ambient dimension. The Green's function for (10), (11) is therefore given by

$$K_A(x, t, s) = K(x + \varphi(t) - \varphi(s), t - s) = \frac{e^{i|x+\varphi(t)-\varphi(s)|^2/4(t-s)}}{(4\pi i(t-s))^{d/2}}, \quad (12)$$

as shown in [1]. We note that the advective nature of the vector potential term is apparent from this viewpoint.

Single and double layer potentials $\mathcal{S}_A[\sigma]$ and $\mathcal{D}_A[\mu]$ may be defined as in (4), (5), (7), (8), with K_A in place of K . For $d > 1$, the double layer potential satisfies the jump condition (9), with \mathcal{D}_A and \mathcal{D}_A^* in place of \mathcal{D} and \mathcal{D}^* . $\mathcal{D}_A^*[\mu]$ again denotes the principal value of $\mathcal{D}_A[\mu]$. For $d = 1$, the jump condition also includes the principle value term, which was identically zero in (6):

$$\lim_{x \rightarrow x_0^\pm} \mathcal{D}_A[\mu](x, t) = \pm \frac{i}{2} \mu(t) + \mathcal{D}_A^*[\mu](t), \quad (13)$$

with

$$\mathcal{D}_A^*[\mu](t) = \frac{\sqrt{i}}{4\sqrt{\pi}} \int_0^t \frac{\varphi(t) - \varphi(s)}{(t-s)^{3/2}} \exp\left(i \frac{(\varphi(t) - \varphi(s))^2}{4(t-s)}\right) \mu(s) ds. \quad (14)$$

The single layer potential $\mathcal{S}_A[\sigma]$ is continuous in both cases.

2.1 Green's identities and TBCs

The following theorem gives TBCs for (1) on an arbitrary bounded domain Ω with a piecewise-smooth boundary. It can be found in slightly different form in [1].

Theorem 1. *Let $x \in \mathbb{R}^d \setminus \overline{\Omega}$ and suppose that u satisfies the free particle Schrödinger equation (3) in this region, with zero initial data. Then for $d > 1$,*

$$iu(x, t) = \mathcal{S}_A \left[\frac{\partial u}{\partial \nu} - i\nu \cdot \mathbf{A}u \right] (x, t) - \mathcal{D}_A[u](x, t). \quad (15)$$

If $x_0 \in \partial\Omega$, excluding non-smooth boundary points, we have

$$\frac{i}{2}u(x_0, t) = \mathcal{S}_A \left[\frac{\partial u}{\partial \nu} - i\nu \cdot \mathbf{A}u \right] (x_0, t) - \mathcal{D}_A^*[u](x_0, t). \quad (16)$$

When $d = 1$, $\Omega = [-x_0, x_0]$, and $x > x_0$, we have

$$iu(x, t) = \mathcal{S}_A \left[\frac{\partial u}{\partial x} - iAu \right] (x, t) + \mathcal{D}_A[u](x, t) \quad (17)$$

and

$$\frac{i}{2}u(x_0, t) = \mathcal{S}_A \left[\frac{\partial u}{\partial x} - iAu \right] (x_0, t) + \mathcal{D}_A^*[u](t). \quad (18)$$

For $x < -x_0$, we have

$$-iu(x, t) = \mathcal{S}_A \left[\frac{\partial u}{\partial x} - iAu \right] (x, t) + \mathcal{D}_A[u](x, t) \quad (19)$$

and

$$-\frac{i}{2}u(-x_0, t) = \mathcal{S}_A \left[\frac{\partial u}{\partial x} - iAu \right] (-x_0, t) + \mathcal{D}_A^*[u](t), \quad (20)$$

with x_0 replaced by $-x_0$ in the definitions of \mathcal{S}_A and \mathcal{D}_A . Here u , $\frac{\partial u}{\partial \nu}$, and $\frac{\partial u}{\partial x}$ refer to their appropriate spatial boundary traces when they are used as arguments to \mathcal{S}_A , \mathcal{D}_A , and \mathcal{D}_A^* , and ν is an outward normal on $\partial\Omega$.

Proof. When $\mathbf{A} \equiv 0$, or $A \equiv 0$, (15), (17), and (19) are Green's identities for the ordinary free-particle Schrödinger equation. These are well-known in the closely-related case of the heat equation [26]. Our proof follows the standard derivation of this Green's identity, modified to include the vector potential term. We only consider the case $d > 1$ here; the proof when $d = 1$ is similar.

Let $s \in [0, t]$ and $x, y \in \mathbb{R}^d \setminus \overline{\Omega}$. Integrating (10) against $K_A(x - y, t, s)$ on $[0, t] \times \mathbb{R}^d \setminus \overline{\Omega}$ gives

$$0 = \int_0^t \int_{\mathbb{R}^d \setminus \overline{\Omega}} K_A(x - y, t, s) [iu_s(y, s) + \Delta u(y, s) - i\mathbf{A}(s) \cdot \nabla u(y, s)] dV(y) ds = T_1 + T_2 + T_3,$$

where we have split the expression into three terms. Integrating T_1 by parts in s gives

$$T_1 = - \int_0^t \int_{\mathbb{R}^d \setminus \overline{\Omega}} i\partial_s K_A(x - y, t, s) u(y, s) dV(y) ds + \int_{\mathbb{R}^d \setminus \overline{\Omega}} i [K_A(x - y, t, s) u(y, s)]_{s=0}^t dV(y).$$

In the first integral, we can compute $\partial_s K_A(x - y, t, s)$ using (12). In the second integral, the boundary term at $s = 0$ vanishes since $u(x, 0) = 0$ in $\mathbb{R}^d \setminus \overline{\Omega}$. For the boundary term at $s = t$, we use the δ -function property of the Green's function. We obtain

$$T_1 = \int_0^t \int_{\mathbb{R}^d \setminus \overline{\Omega}} \left[i \frac{\partial K}{\partial t}(\star, t - s) + i\mathbf{A}(s) \cdot \nabla K(\star, t - s) \right] u(y, s) dV(y) ds + iu(x, t),$$

where we have used the symbol $\star := x - y + \varphi(t) - \varphi(s)$. For T_2 , we use Green's second identity and (12) to obtain

$$T_2 = \int_0^t \int_{\mathbb{R}^d \setminus \bar{\Omega}} \Delta K(\star, t, s) u(y, s) dV(y) ds + \int_0^t \int_{\partial\Omega} \frac{\partial K_A}{\partial \nu_y}(x - y, t, s) u(y, s) - K_A(x - y, t, s) \frac{\partial u}{\partial \nu}(y, s) dS(y) ds.$$

For T_3 , the divergence theorem gives

$$T_3 = - \int_0^t \int_{\mathbb{R}^d \setminus \bar{\Omega}} i \mathbf{A}(s) \cdot \nabla K(\star, t, s) u(y, s) dV(y) ds + \int_0^t \int_{\partial\Omega} i \nu_y \cdot \mathbf{A}(s) K_A(x - y, t, s) u(y, s) dS(y) ds.$$

We now add T_1 , T_2 , and T_3 , and use the fact that K satisfies the free-particle Schrödinger equation (3). After some algebra, we find

$$0 = i u(x, t) + \int_0^t \int_{\partial\Omega} \frac{\partial K_A}{\partial \nu_y}(x - y, t, s) u(y, s) - K_A(x - y, t, s) \left(\frac{\partial u}{\partial \nu}(y, s) - i \nu_y \cdot \mathbf{A}(s) u(y, s) \right) dS(y) ds$$

which is (15). (16) follows from the jump condition (9) and the continuity of the single layer potential by taking the limit as x approaches a smooth boundary point x_0 . \square

Since we have assumed that u_0 and V are supported inside Ω , the identities (16), (18), and (20) hold for (1) and are exact TBCs. To borrow terminology from [2], these may be viewed as generalized Robin conditions, relating the Dirichlet and Neumann data at a time t to those throughout the time history $0 < s < t$. TBCs for the Schrödinger equation in arbitrary piecewise-smooth domains with $\mathbf{A}(t) = 0$ are obtained as a special case. Furthermore, (15), (17), and (19) serve as representation formulas for u outside of Ω , and may be evaluated there if needed.

Remark 2. When $d = 1$ and $A(t) = 0$, $\mathcal{D}_A^* \equiv \mathcal{D}^*$ vanishes and (18) may be written in the form of the standard Neumann-to-Dirichlet (NtD) map:

$$u(x_0, t) = \frac{e^{-3\pi i/4}}{\sqrt{\pi}} \int_0^t \frac{u_x(x_0, s)}{\sqrt{t-s}} ds. \quad (21)$$

The Dirichlet-to-Neumann (DtN) map may be recovered by viewing (21) as an Abel integral equation [25] and solving it explicitly. It is given by

$$\frac{\partial u}{\partial x}(x_0, t) = \frac{e^{3\pi i/4}}{\sqrt{\pi}} \int_0^t \frac{u_t(x_0, s)}{\sqrt{t-s}} ds. \quad (22)$$

Therefore the TBCs above generalize the known DtN and NtD maps, which are derived, for example, in [2, 3] by other means. The conditions for the higher-dimensional cases and/or when $\mathbf{A}(t) \neq 0$ may similarly be written explicitly as DtN or NtD maps involving the inversion of Volterra integral operators. However, as we show in the next section, one can simply discretize the conditions as written to obtain ordinary Robin conditions.

3 Implementation of the TBCs in one dimension

To see how the TBCs presented in the previous section may be used in practice, we describe a simple second-order accurate scheme for the case $d = 1$. The method presented here may be extended to a higher-order discretization in time, and is independent of the choice of spatial discretization in the interior of the domain.

For the right boundary $x = x_0$ of the computational domain, we must discretize (18). We subdivide $[0, T]$ into N equispaced time intervals, and define $t_n = n\Delta t$ with $\Delta t = T/N$. To achieve second-order accuracy, we use a piecewise linear approximation of the solution. In this approximation a function of interest $f(t)$ may be written as

$$f(t) = \sum_{n=1}^N f_n \eta_n(t)$$

with $f_n = f(t_n)$, where $\{\eta_1, \dots, \eta_N\}$ is the standard basis of ‘‘hat’’ functions,

$$\eta_n(t) = \max(1 - |t - t_n|/\Delta t, 0).$$

Note that $\eta_n(t)$ is supported in $[t_{n-1}, t_{n+1}]$. Approximating u and $\frac{\partial u}{\partial x}$ in this way, we obtain a discretization of (18),

$$\left(\frac{i}{2}I_N + iS_N A_N - D_N\right) \mathbf{u}_N - S_N \mathbf{v}_N = 0. \quad (23)$$

Here, I_N is the $n \times n$ identity matrix, A_N is a diagonal matrix with $A_N(n, n) = A(t_n)$,

$$\mathbf{u}_N = [u_1, u_2, \dots, u_N] \approx [u(t_1), u(t_2), \dots, u(t_N)],$$

and

$$\mathbf{v}_N = [v_1, v_2, \dots, v_N] \approx \left[\frac{\partial u}{\partial x}(t_1), \frac{\partial u}{\partial x}(t_2), \dots, \frac{\partial u}{\partial x}(t_N)\right].$$

S_N, D_N are dense lower triangular matrices with

$$S_N(m, n) := \frac{1}{\sqrt{4\pi i}} \int_0^{t_m} \frac{\exp(i(\varphi(t_m) - \varphi(s))^2/4(t_m - s))}{\sqrt{t_m - s}} \eta_n(s) ds \quad (24)$$

$$= \frac{1}{\sqrt{4\pi i}} \int_{\max(0, t_{n-1})}^{\min(t_m, t_{n+1})} \frac{\exp(i(\varphi(t_m) - \varphi(s))^2/4(t_m - s))}{\sqrt{t_m - s}} \eta_n(s) ds, \quad (25)$$

and

$$D_N(m, n) := \frac{\sqrt{i}}{4\sqrt{\pi}} \int_0^{t_m} \frac{\varphi(t_m) - \varphi(s)}{(t_m - s)^{3/2}} \exp\left(i \frac{(\varphi(t_m) - \varphi(s))^2}{4(t_m - s)}\right) \eta_n(s) ds \quad (26)$$

$$= \frac{\sqrt{i}}{4\sqrt{\pi}} \int_{\max(0, t_{n-1})}^{\min(t_m, t_{n+1})} \frac{\varphi(t_m) - \varphi(s)}{(t_m - s)^{3/2}} \exp\left(i \frac{(\varphi(t_m) - \varphi(s))^2}{4(t_m - s)}\right) \eta_n(s) ds. \quad (27)$$

Note that the matrix entries are local in time and can be precomputed using any suitable quadrature scheme. Because of the lower triangular structure of these matrices (a consequence of the fact that the integral operators are of Volterra type), we may write the discrete Green’s identity (23) as

$$\begin{aligned} \left(\frac{i}{2} + iS_N(m, m)A_m - D_N(m, m)\right) u_m - S_N(m, m)v_m = \\ \sum_{n=1}^{m-1} [D_N(m, n)u_n + S_N(m, n)(v_n - iA_n u_n)], \end{aligned} \quad (28)$$

for $m = 1, \dots, N$. These are inhomogeneous Robin boundary conditions for each time step t_m , with the right-hand side involving boundary data from previous time steps.

3.1 Butterfly scheme for the rapid evaluation of the TBCs

The cost of computing the Robin coefficients in (28) naively is of the order $\mathcal{O}(m)$ at the m th time step, and $\mathcal{O}(N^2)$ in total. Thus, without a fast algorithm to apply S_N and D_N , computing the boundary conditions will dominate the asymptotic cost of a simulation in the limit of many time steps.

To develop a fast algorithm, we first partition the matrices S_N and D_N into blocks as in Figure 1, refining blocks towards the diagonal until the dimension of the smallest blocks is a small constant. Rather than applying one row of the matrix per time step, as suggested by the right hand side of (28), we can apply each block as soon as the corresponding entries of \mathbf{u}_N and \mathbf{v}_N become available in the course of time-stepping. The order in which the blocks may be applied is indicated by the numbering in the figure. Each row of the triangular sections near the matrix diagonal (marked in the figure by asterisks) contains at most a constant number of elements, and may be built and applied directly. The results of these matrix-vector and row-vector products may then be arranged and added together as needed to compute the right hand side

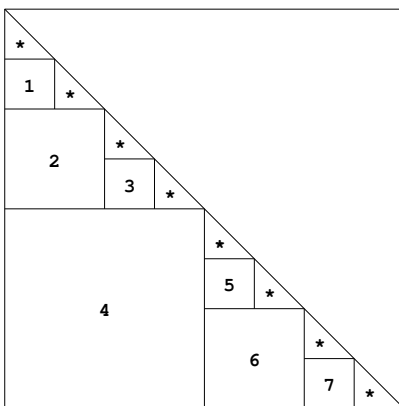


Figure 1: Block partitioning of the matrices S_N and D_N . Numbered blocks are butterfly compressed in advance, and applied in the order indicated. Triangular sections marked by $*$ are applied directly.

of (28). All that is required to overcome the $\mathcal{O}(N^2)$ cost is a suitable method to apply each of the square blocks efficiently.

If the integral operators were convolutional, the fast Fourier transform (FFT) could be used to apply each block in nearly optimal time, as in [27]. In the present case, we replace the FFT with hierarchical *butterfly compression* [28, 29], which is related to the FFT and applies to more general matrices. The only property such matrices require is the so-called “butterfly property” - that the rank of a submatrix is proportional to its area. Butterfly algorithms have been successfully used to compress and apply matrices arising from a variety of special function transforms and oscillatory integral operators. We will not review the literature here, and instead refer the reader to [29, 30, 31]. Since the matrices S_N and D_N are discretizations of an oscillatory integral operator with a smooth phase function, the butterfly algorithm should apply in its standard form.

For each $n \times n$ matrix, the algorithm of [29] begins with an $\mathcal{O}(n^2)$ precomputation step, in which the matrix is compressed as a sparse factorization with only $\mathcal{O}(n \log n)$ nonzero elements. Afterward, the matrix may be applied at a cost of $\mathcal{O}(n \log n)$. We use this algorithm for each block. Summing the costs from large to small blocks, we find the total precomputation cost is

$$\frac{N}{2} + 2 \left(\frac{N}{4} \right)^2 + 4 \left(\frac{N}{8} \right)^2 + \dots \sim \mathcal{O}(N^2).$$

The total matrix apply and memory storage costs are

$$\frac{N}{2} \log \frac{N}{2} + 2 \left(\frac{N}{4} \log \frac{N}{4} \right) + 4 \left(\frac{N}{8} \log \frac{N}{8} \right) + \dots \sim \mathcal{O}(N \log^2 N),$$

since there are $\mathcal{O}(\log N)$ terms in the sum. The precomputation for S_N and D_N must be performed once for each choice of $A(t)$, Δt , and T , but does not depend on V , u_0 , x_0 , or any spatial discretization parameters. The scheme is therefore particularly efficient when one wishes, for example, to fix $A(t)$ and solve the Schrödinger equation for multiple initial conditions u_0 and potentials V .

The butterfly “compressibility” of various classes of matrices is an area of ongoing research, and we will not undertake a theoretical analysis of the rank properties of S_N and D_N here. The reader will find discussions of this topic for several classes of matrices in the aforementioned references. All of our numerical experiments indicate that S_N and D_N are butterfly compressible even for large-amplitude vector potentials, and that the algorithm performs efficiently and with the expected scaling, as will be demonstrated in the following section.

4 Numerical examples

To demonstrate the effectiveness of our transparent boundary condition in the one-dimensional case with $A(t) \neq 0$, we discretize (2), with $\Omega = [-x_0, x_0]$, by a Crank-Nicolson scheme coupled to the Robin condition (28). The resulting method is second-order accurate in the time step Δt and the grid spacing Δx .

4.1 Example 1: Gaussian wavepacket with $V = 0$

For our first example, we set $x_0 = 1$, $V = 0$, and take u_0 to be a Gaussian wavepacket,

$$u_0(x) = \frac{1}{\sqrt{\alpha}} e^{ik(x-\mu)} e^{-(x-\mu)^2/4\alpha^2}, \quad (29)$$

with $\alpha = 0.08$, $k = -10$, and $\mu = 0$, so that the support of u_0 is contained in Ω to at least fourteen digits of accuracy. The potential $A(t)$ is taken to be a pulse

$$A(t) = A_0 \sin^2(t\pi/T) \cos(\omega t) \quad (30)$$

with $A_0 = 3000$, $\omega = 300$, and $T = 0.1$. The indefinite integral φ may be computed analytically. The wavepacket is advected approximately $\max |\varphi| \approx 10$ domain radii from the origin at its maximal excursion, sweeping it back and forth across the domain in several cycles. Figure 2 shows the absolute value of a numerical solution obtained using the TBCs, along with $A(t)$. A video of the solution is available at the webpage: https://cims.nyu.edu/~kaye/kg_tbcse1_ex.html.

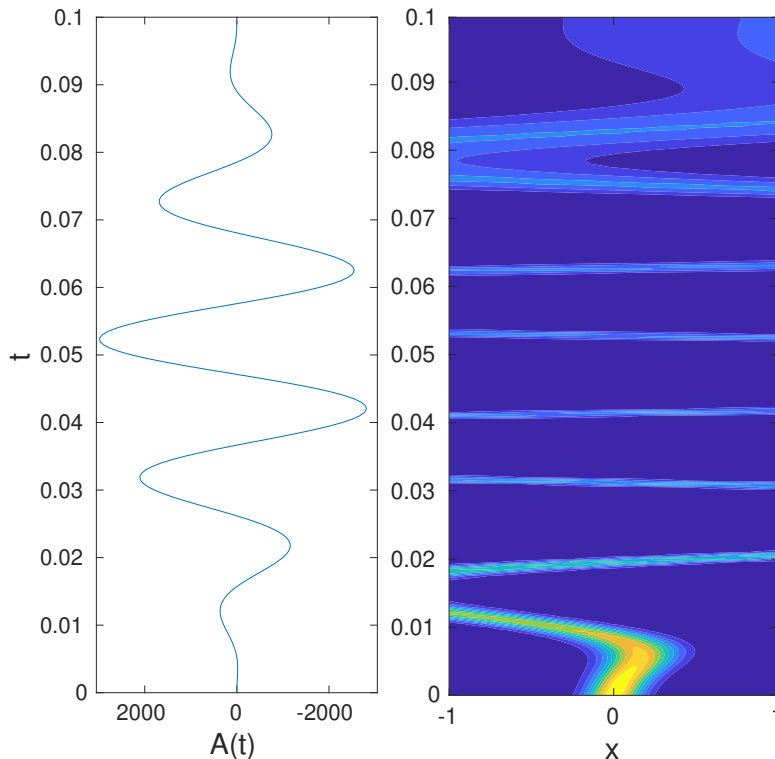


Figure 2: Plots of $A(t)$ and $|u(x,t)|$ for Example 1, with time on the vertical axis. The horizontal axis has been reversed in the first plot so that the sign of $A(t)$ lines up with the direction of advection. As the wavepacket disperses, it is pushed rapidly back and forth across the domain by the applied field, causing it to leave and return repeatedly. At its maximal excursion, the center of the wavepacket is approximately 10 domain radii from the origin.

Since the solution of the free-particle Schrödinger equation with Gaussian wavepacket initial data is known analytically, the solution for our case may be obtained by shifting it by φ . We can therefore measure the error directly. We first demonstrate that the entire discretization scheme is second-order in Δt . The scheme

is also second-order in Δx , but we focus on the convergence in Δt since this includes the discretization error of the boundary condition. We fix Δx sufficiently small so that the influence of the spatial discretization is eliminated, and compute the numerical solution for several choices of Δt . For each one, we compute the maximum L^2 error on $[-1, 1]$ over the duration of the simulation. The results, given in Table 1, demonstrate the desired convergence rate.

In order to isolate any discretization error caused by the boundary condition, we solve the PDE using the Crank-Nicolson scheme on the domain $[-20, 20]$ with the Robin condition replaced by zero Dirichlet boundary conditions. These are correct to machine precision for this case. We use the same fixed Δx as before, and again measure the maximum L^2 error on $[-1, 1]$ for the same choices of Δt . The results, also given in Table 1, show that for the same Δt , the TBC scheme is actually more accurate than the brute force scheme.

Δt	1×10^{-5}	5×10^{-6}	2.5×10^{-6}	1.25×10^{-6}	6.25×10^{-7}
TBC	2.62×10^{-1}	6.61×10^{-2}	1.67×10^{-2}	4.21×10^{-3}	1.09×10^{-3}
DBC	7.29×10^{-1}	2.12×10^{-1}	5.43×10^{-2}	1.37×10^{-2}	3.49×10^{-3}

Table 1: Maximum L^2 error of the Gaussian wavepacket solution on $[-1, 1]$ for recursively halved values of Δt and fixed $\Delta x = 2 \times 10^{-4}$, using the transparent boundary condition scheme (TBC) as well as homogeneous Dirichlet boundary conditions on a much larger domain (DBC).

We next measure the total time required to compute the TBCs, first by applying rows of S_N and D_N directly, and then by using the butterfly scheme described in Section 3.1. The matrices S_N and D_N are precomputed and butterfly compressed beforehand. Table 2 shows the time spent on finite difference marching and the time spent computing boundary conditions. The cost of obtaining TBCs using the butterfly scheme appears to scale sublinearly with N for the values tested, and represents a negligible part of the total cost of the simulation. With the direct scheme, this cost scales like $O(N^2)$, and eventually overtakes the cost of marching.

$N = T/\Delta t$	10,000	20,000	40,000	80,000	160,000
Time for finite difference marching	4.9	9.7	19.4	39.0	78.2
Time to obtain TBCs (direct)	0.42	1.68	6.81	28.02	120.90
Time to obtain TBCs (butterfly)	0.17	0.29	0.42	0.66	1.25

Table 2: Wall clock timings, in seconds, for Crank-Nicolson marching, and for obtaining TBCs with and without the butterfly scheme. Recursively doubled values of N correspond to the values of Δt shown in Table 1.

Remark 3. *As mentioned above, the timings in Table 2 do not include the construction and/or compression of S_N and D_N . In the direct application scheme, the cost of building these matrices is $O(N^2)$. The memory required to store them is also $O(N^2)$, so for sufficiently large N one must build them on the fly. The cost of this step cannot be shared over many simulations, and would be a significant addition to the costs reflected in the table. In the butterfly scheme, the cost of building and compressing the matrices is $O(N^2)$, but the memory required to store them is only $O(N \log^2 N)$. Therefore the matrices may be built, compressed, and stored, once for each choice of T , $A(t)$, and Δt , thereby eliminating any online cost associated with matrix construction.*

4.2 Examples 2-4: Gaussian wavepacket interacting with a repulsive potential

Our second set of examples demonstrates the case $V \neq 0$, and shows that the same precomputed and compressed integral operators may be used for a series of simulations with several different choices of V . We again take u_0 to be a Gaussian wavepacket (29), now with $\alpha = 0.08$, $k = 0$, and $\mu = -2$. We define $A(t)$ as in (30), with $A_0 = -220$, $\omega = 0$, and $T = 0.1$. We then let V be a Gaussian centered at the origin:

$$V(x) = V_{\max} e^{-x^2/2\beta^2},$$

with $\beta = 0.1$. V_{\max} is taken to be 4000, 6000, or 8000. We choose $\Omega = [-3, 3]$, so that V and u_0 are zero to machine precision outside of Ω .

In each example, the Gaussian wavepacket is advected to the right and interacts with the potential barrier V . Some of the incident wavepacket is reflected, and some transmitted, depending on V_{\max} . The reflected and transmitted waves then exit the domain through the transparent boundaries. The absolute value of each solution and the vector potential $A(t)$ are shown in Figure 3. Videos of each solution are available at the URL mentioned in Section 4.1 above.

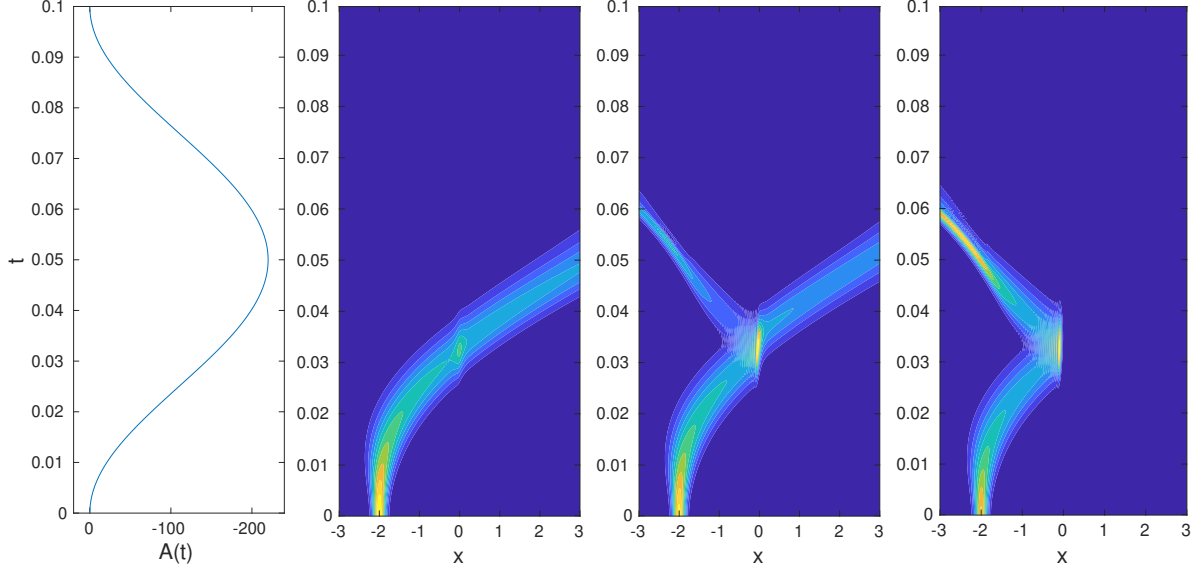


Figure 3: Plots of $A(t)$ and $|u(x, t)|$, displayed in the order $V_{\max} = 4000, 6000, 8000$, for Examples 2-4. The wavepacket is accelerated towards the potential barrier. Its reflection coefficient depends on V_{\max} . After it interacts with the barrier, the reflected and transmitted waves leave the domain.

In this case, no analytical solution is available, so we measure the error against highly accurate numerical solutions obtained using an alternative discretization scheme, as follows. The PDE is semidiscretized in time using the trapezoidal rule, and coupled to the Robin condition (28), with a very small time step Δt . At each time step, this gives an elliptic two-point boundary value problem with Robin conditions, which we solve using a non-adaptive version of the high-order scheme described in [32]. We then sample this solution on the Crank-Nicolson grid, and take it as our reference.

Before running any simulations, we compress the matrices S_N and D_N , with several choices of Δt , for use in all three examples. We repeat the convergence tests from Example 1 to demonstrate the second-order accuracy of the overall scheme in Δt . The results are shown in Table 3. As before, for each example, we compare the TBC scheme to a Crank-Nicolson scheme with zero Dirichlet boundary conditions on the domain $\Omega = [-25, 25]$, which contains the support of each solution to machine precision. The same fixed Δx is used in both cases. The errors are very similar for both schemes. We speculate that the TBC scheme is more accurate than the brute force scheme in Example 1 because the latter accumulates errors outside of Ω , which are then reintroduced once the sign of $A(t)$ reverses. In Examples 2-4, the sign of $A(t)$ does not change, so the same mechanism does not arise. This combination of results suggests that the discretization error contributed by the TBC tends to be smaller than that of the overall finite difference scheme.

Δt	2×10^{-5}	1×10^{-5}	5×10^{-6}	2.5×10^{-6}	1.25×10^{-6}
$V_{\max} = 4000$, TBC	6.56×10^{-3}	1.64×10^{-3}	4.11×10^{-4}	1.03×10^{-4}	2.58×10^{-5}
$V_{\max} = 4000$, DBC	6.56×10^{-3}	1.64×10^{-3}	4.11×10^{-4}	1.03×10^{-4}	2.57×10^{-5}
$V_{\max} = 6000$, TBC	3.45×10^{-1}	8.77×10^{-2}	2.20×10^{-2}	5.60×10^{-3}	1.49×10^{-3}
$V_{\max} = 6000$, DBC	3.45×10^{-1}	8.77×10^{-2}	2.20×10^{-2}	5.60×10^{-3}	1.49×10^{-3}
$V_{\max} = 8000$, TBC	6.45×10^{-1}	1.64×10^{-1}	4.12×10^{-2}	1.05×10^{-2}	2.80×10^{-3}
$V_{\max} = 8000$, DBC	6.45×10^{-1}	1.64×10^{-1}	4.12×10^{-2}	1.05×10^{-2}	2.80×10^{-3}

Table 3: Maximum L^2 errors on $[-3, 3]$ versus Δt for Examples 2-4. $\Delta x = 9.375 \times 10^{-6}$ is fixed throughout.

In Table 4, we give timings for Crank-Nicolson marching and for computing the TBCs using the butterfly scheme. Timings are only shown for one of the three examples, since they are all similar. The results demonstrate near-linear scaling of the butterfly scheme. We note that in this case, the total time required to compute the TBCs is significantly less than in the first example, remaining under 0.02% of the total simulation cost for all choices of N . This is most likely a consequence of the simpler structure of $A(t)$, which leads to more compressible S_N and D_N matrices.

$N = T/\Delta t$	5,000	10,000	20,000	40,000	80,000
Time for finite difference marching	167	340	677	1347	2679
Time to obtain TBCs (butterfly)	0.0255	0.0566	0.1226	0.2563	0.5123

Table 4: Wall clock timings, in seconds, for the example with $V_{max} = 8000$; these are typical for Examples 2-4.

5 Conclusions

We have presented a derivation of simple TBCs for the Schrödinger equation with a vector potential in an arbitrary domain with a piecewise smooth boundary. For the one-dimensional case with $A(t) = 0$, these reduce to the well-known exact nonlocal conditions. When $A(t) \neq 0$, the conditions become non-convolutional, and we have developed a fast “butterfly” scheme to implement them. In order to reduce the computational complexity of the precomputation phase of our scheme, it would be useful to explore recent variants of the butterfly algorithm, such as [31], which address this issue.

In higher-dimensions, more elaborate fast and memory-efficient algorithms will be required to make exact TBCs conditions practical for large-scale problems. This work is in progress, and will be presented at a later date.

Acknowledgments

We would like to thank Alex Barnett, Angel Rubio, Umberto De Giovannini, Hannes Hübener, Michael Ruggenthaler, and Mike O’Neil for many useful conversations. Jason Kaye was supported in part by the Research Training Group in Modeling and Simulation funded by the National Science Foundation via grant RTG/DMS - 1646339.

References

- [1] A. M. Ermolaev, I. V. Puzynin, A. V. Selin, and S. I. Vinitzky, “Integral boundary conditions for the time-dependent Schrödinger equation: Atom in a laser field,” *Phys. Rev. A*, vol. 60, no. 6, p. 4831, 1999.
- [2] V. A. Baskakov and A. V. Popov, “Implementation of transparent boundaries for numerical solution of the Schrödinger equation,” *Wave Motion*, vol. 14, no. 2, pp. 123–128, 1991.
- [3] S. Jiang and L. Greengard, “Fast evaluation of nonreflecting boundary conditions for the Schrödinger equation in one dimension,” *Comput. Math. Appl.*, vol. 47, no. 6, pp. 955–966, 2004.
- [4] C. Lubich and A. Schädle, “Fast convolution for nonreflecting boundary conditions,” *SIAM J. Sci. Comput.*, vol. 24, pp. 161–182, 2002.
- [5] A. Schädle, M. López-Fernández, and C. Lubich, “Fast and oblivious convolution quadrature,” *SIAM J. Sci. Comput.*, vol. 28, no. 2, pp. 421–438, 2006.
- [6] T. Hagstrom, “Radiation boundary conditions for the numerical simulation of waves,” *Acta Numer.*, vol. 8, pp. 47–106, 1999.
- [7] S. Jiang and L. Greengard, “Efficient representation of nonreflecting boundary conditions for the time-dependent Schrödinger equation in two dimensions,” *Commun. Pure Appl. Math.*, vol. 61, no. 2, pp. 261–288, 2008.
- [8] H. Han and Z. Huang, “Exact artificial boundary conditions for the Schrödinger equation in \mathbb{R}^2 ,” *Commun. Math. Sci.*, vol. 2, no. 1, pp. 79–94, 2004.
- [9] H. Han, D. Yin, and Z. Huang, “Numerical solutions of Schrödinger equations in \mathbb{R}^3 ,” *Numer. Methods Partial Differ. Equ.*, vol. 23, no. 3, pp. 511–533, 2007.
- [10] X. Antoine, A. Arnold, C. Besse, M. Ehrhardt, and A. Schädle, “A review of transparent and artificial boundary conditions techniques for linear and nonlinear Schrödinger equations,” *Commun. Comput. Phys.*, vol. 4, no. 4, pp. 729–796, 2008.

- [11] A. Schädle, “Non-reflecting boundary conditions for the two-dimensional Schrödinger equation,” *Wave Motion*, vol. 35, no. 2, pp. 181–188, 2002.
- [12] R. M. Feshchenko and A. V. Popov, “Exact transparent boundary condition for the parabolic equation in a rectangular computational domain,” *J. Opt. Soc. Am. A*, vol. 28, pp. 373–380, 2011.
- [13] R. M. Feshchenko and A. V. Popov, “Exact transparent boundary condition for the three-dimensional Schrödinger equation in a rectangular cuboid computational domain,” *Phys. Rev. E*, vol. 88, p. 053308, 2013.
- [14] V. Vaibhav, “On the nonreflecting boundary operators for the general two dimensional Schrödinger equation,” *arXiv*, vol. 1502.04519, 2015.
- [15] A. Arnold, M. Ehrhardt, and I. Sofronov, “Discrete transparent boundary conditions for the Schrödinger equation: fast calculation, approximation and stability,” *Commun. Math. Sci.*, vol. 1, no. 3, pp. 501–556, 2003.
- [16] A. Arnold, M. Ehrhardt, M. Schulte, and I. Sofronov, “Discrete transparent boundary conditions for the Schrödinger equation on circular domains,” *Commun. Math. Sci.*, vol. 10, no. 3, pp. 889–916, 2012.
- [17] S. Ji, Y. Yang, G. Pang, and X. Antoine, “Accurate artificial boundary conditions for the semi-discretized linear Schrödinger and heat equations on rectangular domains,” *Comput. Phys. Commun.*, vol. 222, pp. 84–93, 2018.
- [18] V. Vaibhav, “Transparent boundary condition for numerical modeling of intense laser-molecule interaction,” *J. Comput. Phys.*, vol. 283, pp. 478–494, 2015.
- [19] R. M. Feshchenko and A. V. Popov, “Exact transparent boundary conditions for the parabolic wave equations with linear and quadratic potentials,” *Wave Motion*, vol. 68, pp. 202–209, 2017.
- [20] X. Antoine, E. Lorin, and Q. Tang, “A friendly review of absorbing boundary conditions and perfectly matched layers for classical and relativistic quantum waves equations,” *Mol. Phys.*, vol. 115, no. 15-16, pp. 1861–1879, 2017.
- [21] U. De Giovannini, A. H. Larsen, and A. Rubio, “Modeling electron dynamics coupled to continuum states in finite volumes with absorbing boundaries,” *Eur. Phys. J. B*, vol. 88, no. 3, p. 56, 2015.
- [22] M. Weinmüller, M. Weinmüller, J. Rohland, and A. Scrinzi, “Perfect absorption in Schrödinger-like problems using non-equidistant complex grids,” *J. Comput. Phys.*, vol. 333, pp. 199–211, 2017.
- [23] E. Lorin, S. Chelkowski, and A. Bandrauk, “Mathematical modeling of boundary conditions for laser-molecule time-dependent Schrödinger equations and some aspects of their numerical computation one-dimensional case,” *Numer. Methods Partial Differ. Equ.*, vol. 25, no. 1, pp. 110–136, 2009.
- [24] E. N. Economou, *Green’s functions in Quantum Physics*. Springer, Berlin, 2006.
- [25] W. Pogorzelski, *Integral equations and their applications*. Pergamon Press, 1966.
- [26] R. B. Guenther and J. W. Lee, *Partial Differential Equations of Mathematical Physics and Integral Equations*. Prentice Hall, 1988.
- [27] E. Hairer, C. Lubich, and M. Schlichte, “Fast numerical solution of nonlinear Volterra convolution equations,” *SIAM J. Sci. Stat. Comp.*, vol. 6, no. 3, pp. 532–541, 1985.
- [28] E. Michielssen and A. Boag, “A multilevel matrix decomposition algorithm for analyzing scattering from large structures,” *IEEE Trans. Antennas Propag.*, vol. 44, p. 10861093, 1996.
- [29] M. O’Neil, F. Woolfe, and V. Rokhlin, “An algorithm for the rapid evaluation of special function transforms,” *Appl. Comput. Harmon. Anal.*, vol. 28, no. 2, pp. 203–226, 2010.
- [30] E. Candès, L. Demanet, and L. Ying, “A fast butterfly algorithm for the computation of Fourier integral operators,” *Multiscale Model. Simul.*, vol. 7, no. 4, pp. 1727–1750, 2009.
- [31] Y. Li, H. Yang, E. Martin, K. L. Ho, and L. Ying, “Butterfly factorization,” *Multiscale Model. Simul.*, vol. 13, pp. 714–732, 2015.
- [32] J.-Y. Lee and L. Greengard, “A fast adaptive numerical method for stiff two-point boundary value problems,” *SIAM J. Sci. Comput.*, vol. 18, no. 2, pp. 403–429, 1997.